Peer-reviewed version available at *Appl. Sci.* **2018**, *8*, 2105; doi:10.3390/app8112105

Article

The Influence of Crack Modes on the Elastic Wave Propagation Characteristics in a Non-uniform Rotating Shaft

Yimin Wei[1], Xuan Shi[1], Qi Liu[1] and Wenhua Chen[1,*]

[1] National and Local Joint Engineering Research Center of Reliability Analysis and Testing for Mechanical and Electrical Products, Zhejiang Sci-Tech University, Hangzhou, 310016, P. R. China; yiminwei@126.com

[*] Correspondence: chenwh@zstu.edu.cn; Tel.: +86-571-86843007

Abstract: The vibration propagates in a media such as a shaft in the form of elastic waves. The propagation characteristics of the waves are affected by the geometry of the media, the material properties as well as the cracks. The study to elastic waves propagating in a shaft with transverse cracks can help to detect them. The transverse crack possesses different crack modes due to different external loads. The influence of the crack mode, the location and the depth to the propagation characteristics is investigated in this paper. Firstly, the local flexibility coefficients with three different modes are deduced. And then, the transfer matrix of the elastic wave can be obtained. Finally, the influence of the crack mode, the location and the depth of the transverse crack as well as the rotating speed to the propagation characteristics is then studied, both in a numerical and an experimental way. It's found that mode III is the most suitable mode in this paper, the location of the crack will make the stopbands fluctuating, the depth mainly affects the bandwidth of the stopbands, and the increase of the rotating speed will shift up the stopbands without changing their bandwidths.

Keywords: propagation characteristic; crack modes; elastic waves; rotating shaft; bandwidth

1. Introduction

Rotating machinery are extensively used in today's industries and a crack in a rotating shaft can cause a costly failure, even a heavy accident [1]. The detection of cracks in structures is a very important issue in many real practices, such as power plants, automobiles etc. and more effective detection methods allowing to assess the location and depth of the cracks are continuously investigated [2-4]. The vibration of the shaft can activate the elastic waves, the propagation characteristics of which are affected by the transverse cracks. The relationship between the cracks and the propagation characteristics of the elastic waves has drawn wide attention [5,6].

In the past few decades, vibration-based analysis methods are often used to study the dynamics of the cracked shaft in a rotating machine [7-10]. Usually, the vibration propagates in a shaft in the form of elastics waves, and the propagation characteristics of which are affected by the geometrical dimensions of the shaft, the rotating speed, as well as the transverse cracks. Wave-based damage detection techniques are employed prevalently in the health-monitoring of structural components. Wave method has been used for many applications in 1-D structure [11], in a plate [12], in metamaterial rods [13], in a square pile [14] and in a non-uniform cross-section piles [15] etc. In particular, techniques exploiting wave-damage interactions have received an increasing attention in the recent past, because of the advantages that they offer over the conventional techniques in terms of robustness and higher sensitivity [16,17].

When studying the crack with the elastic wave method, the transfer matrix is often used to indicate the propagation process of the waves [18], and in which the transverse cracks are often model as local springs [2,18,19]. The stiffness coefficient of the local spring is determined by the flexibility of the crack tips, i.e. the crack modes, which have been studied widely [20-22]. Usually, the

Peer-reviewed version available at Appl. Sci. 2018, 8, 2105; doi:10.3390/app8112105

transverse cracks on the rotating shaft possesses different crack modes due to the different external loads, and there are three typical modes: opening mode (mode I), edge-sliding mode (mode II) and tearing mode (mode III) [23]. Many studies about the crack modes and crack detection can be found. Under general mixed mode I/II/III loading, Saboori et al. [24] extended a two stress-based failure criteria to study brittle fracture in engineering components weakened by a blunt V-notch. Isidoro et al. [25] analyzed the influence of bending and torsion on the Stress Intensity Factors (SIF), $K_{I,II,III}$, at different crack geometries. Predan et al. [26] calculated the stress-intensity factor for the circumferential semi-elliptical surface cracks in a hollow cylinder's cross section under torsion using a finite-element technique. With only considering the crack mode I, the authors of this paper also studied the propagation characteristics of the elastic waves in a non-uniform shaft by using the transfer matrix method [27,28].

The crack modes will affect the local flexibility of the transverse crack which is modeled as a local spring, thus, the characteristics of the transfer matrix for the elastic waves will be affected. Former studies have shown the influence of the geometry of the shaft as well as the rotating speed to the propagation characteristics of the elastic waves, which can provide a basis to study the crack. The depth and location of the transverse cracks do affect the propagation characteristics of the elastic waves propagating in the shaft. For a real application, the mode II and mode III do exist, thus, it's necessary to study the propagation characteristics with different modes.

The influence of different crack modes, the location and depth of the transverse crack as well as the rotating speed to the propagation characteristics is studied in this paper. The local stiffness coefficients are deduced firstly under different external loads with only considering an individual mode in Section 2. In Section 3, the transfer matrix equation is built. The most suitable mode is then chosen out. With the chosen mode, the relationship between the propagation characteristics and the location, the depth of the crack, as well as the rotating speed are studied both in a numerical and experimental method. A conclusion and discussion are made in Section 4.

2. Theoretical study

2.1 Transfer matrix for a shaft with transverse cracks

A rotating shaft is often with variable cross-section area, see Figure 1. There are several transverse cracks, E is the elastic modulus, ρ is the density of the shaft, v is the Poisson's ratio and L is the length. As can be seen in Figure 1(a), the area of the cross-section of the shaft $S(x)$ varies as the location of the x-axis. Usually, the motion status of the elements on the shaft can be expressed by a state vector $\mathbf{y} = [u \ \phi \ Q \ M]^{\mathrm{T}}$, where, u, ϕ, Q, M indicate displacement, slope, force and moment for a shaft [28]. Here, the two vectors $\mathbf{y}_0$, $\mathbf{y}_l$ are used to indicate the status of location x_0 and x_l, separately. Suppose that there are n transverse cracks, locating at x_{c1}, …x_{ci}…x_{cn}, the shaft is divided into n+1 segments, see Figure 1(b).

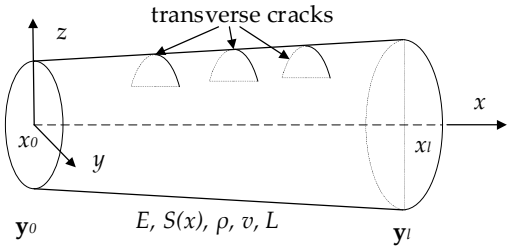

(a)

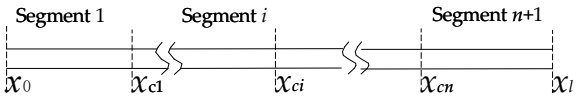

(b)

Figure 1. A schematic of a non-uniform shaft with transverse cracks, the cross section varies as the location of x, as shown in (a), the shaft is divided into n+1 segments by n transverse cracks, as shown in (b).

As for the transverse cracks shown in Figure 1, the deformation of the crack varies, even though for the same material and with the same external conditions. And usually, the crack modes can be divided into three typical mode: opening mode (mode I), edge-sliding mode (mode II) and tearing mode (mode III) according to the departure type, the external loads and the deformation, see Figure 2 [23].

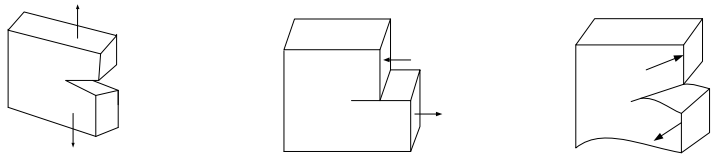

(a) (b) (c)

Figure 2. Three typical crack modes, (a) is the opening mode (mode I), (b) is the edge-sliding mode (mode II) and (c) is the tearing mode (mode III).

As shown in Figure 1, suppose that the elastic waves propagate from location x_0 (x=0) to location x_l (x=L), the propagation process can be expressed by [28]:

$$\mathbf{y}(x_l) = \mathbf{T}\mathbf{y}(x_0) \tag{1}$$

where, **T** is the transfer matrix. Suppose the i-th eigenvalues of the matrix **T** to be λ_i , and the eigenvalue λ_i is usually a complex number and can be expressed as $\lambda_i = e^{\mu_i}$, where $\mu_i = \alpha_i + j\beta$ is known as the propagation constants, $j = \sqrt{-1}$, α_i is called as the attenuation factor indicating the attenuation of the amplitude of the elastic waves varies as the frequency, β_i is the phase angle indicating the phase difference of the wave components during propagation. When the phase angle β_i equals 0 or $\pm\pi$, it means that the transmitted waves encounters the reflected ones cancelling out each other and the waves with corresponding frequencies couldn't pass through the shaft [29].

As shown in Figure 1(b), the shaft is divided into n+1 segments. For the i-th segment, the transfer matrix can be written as

$$\mathbf{T}_i = \mathbf{G}(x_i) e^{\int_0^{L_i} \mathbf{H}(x)dx} \mathbf{G}(x_{i-1})^{-1} \tag{2}$$

where, **H**(x), **G**(x) are:

$$\mathbf{H}(x) = \begin{bmatrix} 0 & 1 & 0 & 0 \\ 0 & 0 & 0 & 1 \\ \dfrac{\rho S(x)\omega^2}{EI(x)} & 0 & 0 & -\dfrac{\rho I(x)\Omega + EI(x)_{,xx}}{EI(x)} \\ 0 & 0 & 1 & 0 \end{bmatrix}, \quad \mathbf{G}(x) = \begin{bmatrix} 1 & 1 & 0 & 0 \\ 0 & 1 & 0 & 0 \\ 0 & 0 & -EI(x) & 0 \\ 0 & 0 & 0 & EI(x) \end{bmatrix},$$ where, $I(x)$ is the inertia momentum at location x, ω is the angular frequency of the components of the elastic waves. For the transverse cracks in a single non-uniform shaft, it's often treated as a local spring [2]. And the transfer matrix for the i-th crack can be written as: $\mathbf{C}_i = \begin{bmatrix} 1 & 0 & 0 & 0 \\ 0 & 1 & 0 & c_i \\ 0 & 0 & 1 & 0 \\ 0 & 0 & 0 & 1 \end{bmatrix}$, where, c_i is the local stuffiness coefficient of the transverse crack, i.e. the stiffness coefficient of the local spring. c_i is determined by the crack modes. It can be inferred that the transfer matrix for the whole shaft is [28]:

$$\mathbf{T} = \mathbf{T}_{n+1}\mathbf{C}_n \ldots \mathbf{T}_i\mathbf{C}_i \ldots \mathbf{C}_1\mathbf{T}_1 \tag{3}$$

Equation (3) is the transfer matrix for the non-uniform rotating shaft with n transverse cracks, the eigenvalues of which can be used to indicate the propagation characteristics of the elastic waves.

2.2 Local stiffness coefficient

Figure 3 is a schematic of the transverse crack, Figure 3(a) is the free body diagram, and P_1, P_1', P_2, P_2', P_3, P_3' are the external loads that the shaft suffering. Figure 3(b) is the section view of the crack, where, a is the crack depth, the width of the crack is $2b$, $\boldsymbol{R}_c$ is the radius of cross-section. The crack mode is determined by the external loading $P_1, P_1', P_2, P_2', P_3, P_3'$.

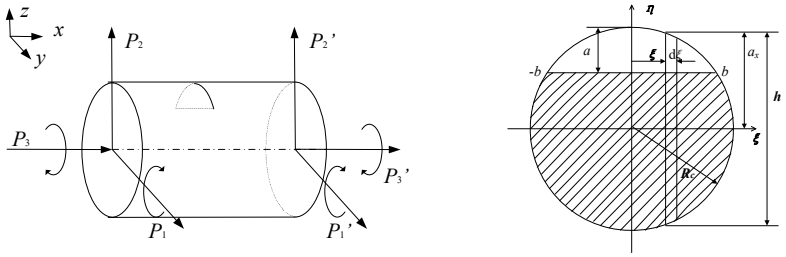

(a) (b)

Figure 3. A schematic of the transverse crack, (a) is the free body diagram and (b) is the section view of the crack.

The additional strain energy U_c and the additional displacement u_i^c of the transverse crack shown in Figure 3 can be expressed in the following way [30]:

$$U_c = \int_A J(A)dA,\ u_i^c = \frac{\partial U_c}{\partial P_i} \tag{4}$$

where, A is the area of the crack shown in Figure 3(b), $J(A)$ is the strain energy density function, which can be expressed as:

$$J(A) = \frac{1-\nu^2}{E} K_n^{\ 2} \tag{5}$$

where, K_n (n=I, II, III) is the stress-intensity factor with three different crack modes. According to the definition, the local stiffness coefficients can be written as:

$$c_i = \frac{\partial u_i^c}{\partial P_i} = \frac{\partial^2}{\partial P_i \partial P_i} \int_0^a \int_{-b}^b J(A)d\xi d\eta \tag{6}$$

where, i is the index of the external loading. Equation (6) is the equation for the local stiffness coefficients, substituting related loadings into which, the coefficients can be obtained.

For mode I, only the loadings P_1 and P_1' are needed to be considered, see Figure 3(b). It can be deduced that the local stiffness coefficient along the crack direction is [31]

$$c_1 = 2\frac{1-\nu^2}{E} \int_0^b \int_0^\eta \frac{32}{\pi R^8} (R^2 - \xi^2)\eta F_1^2(\eta/h) d\eta d\xi \tag{7}$$

where, h is the height of infinitesimal local area, and $h = 2\sqrt{R^2 - \xi^2}$, $F_1(\eta/h) = 1.125 + 1.4(\eta/h) + 7.33(\eta/h)^2 + 13.08(\eta/h)^3 + 14(\eta/h)^4$.

For mode II, only the loadings P_2 and P_2' are needed to be considered. And $K_{II2} = \frac{kP_2}{\pi R^2}\sqrt{\pi\eta} F_{II}\left(\frac{\eta}{h}\right)$, $k = 6(1+\nu)/(7+6\nu)$, substituting all the related parameters into Equation (6), it can be deduced that

$$c_2 = \frac{\partial u_i^c}{\partial P_i} = \frac{\partial^2}{\partial P_1 \partial P_1}\int_{-b}^{b}\int_0^{\eta} J(A)\,d\eta\,d\xi$$
$$= 2\frac{1-\nu^2}{E}\frac{36(1+\nu)^2}{(7+6\nu)^2}\int_{-b}^{b}\int_0^{\eta}\frac{\eta}{\pi R^4}F_{\mathrm{II}}^2\left(\frac{\eta}{h}\right)d\eta\,d\xi \tag{8}$$

where, $\eta = (a-R)+\sqrt{R^2-\xi^2}$, $F_{\mathrm{II}}(\eta/h) = \dfrac{1.122-0.561(\eta/h)+0.085(\eta/h)^2+0.18(\eta/h)^3}{\sqrt{1-(\eta/h)}}$.

Considering that Equation (8) is even symmetric, thus it can be further written as

$$c_2 = 4\frac{1-\nu^2}{E}\frac{36(1+\nu)^2}{(7+6\nu)^2}\int_0^{b}\int_0^{\eta}\frac{\eta}{\pi R^4}F_{\mathrm{II}}^2\left(\frac{\eta}{h}\right)d\eta\,d\xi \tag{9}$$

For mode III, as mentioned before, the strain energy density function and stress stiffness factor can be expressed as:

$$J(A) = \frac{(1-\nu^2)(1+\nu)}{E}K_{\mathrm{III}}{}^2 \tag{10}$$

$$K_{\mathrm{III}} = \frac{P_2}{\pi R^4}\sqrt{R^2-\xi^2}\sqrt{\pi\eta}F_{\mathrm{III}}(\frac{\alpha}{h}) \tag{11}$$

Substituting Equations (10) and (11) into Equation (6), the local stiffness coefficient along the crack direction is obtained

$$c_3 = \frac{\partial u_i^c}{\partial P_i} = \frac{\partial u_2^c}{\partial P_3} = \frac{\partial^2}{\partial P_3^2}\int_{-b}^{b}\int_0^{\eta} J(A)\,d\eta\,d\xi$$
$$= \frac{2(1-\nu^2)(1+\nu)}{E}\int_{-b}^{b}\int_0^{\eta}\frac{1}{\pi R^8}(R^2-\xi^2)\eta F_{\mathrm{III}}{}^2(\eta/h)\,d\eta\,d\xi \tag{12}$$

where, $F_{\mathrm{III}}(\eta/h) = \sqrt{(2h/\pi\eta)\tan(\pi\eta/2h)}$. Similarly, considering that the equation is even symmetric, thus Equation (12) can be further written as

$$c_3 = \frac{4(1+\nu)(1-\nu^2)}{E}\int_0^{b}\int_0^{\eta}\frac{(R^2-\xi^2)}{\pi R^8}\eta F_{\mathrm{III}}^2(\eta/h)\,d\eta\,d\xi \tag{13}$$

Substituting Equations (7), (8) or (12) into Equation (3) separately, the transfer matrix of the elastic wave with different crack mode can then be deduced. Further, the eigenvalues of the transfer matrix can be studied, and then the propagation characteristics of the elastic waves can be obtained.

3. Numerical Simulation & Experimental Analysis

It can be seen the transfer matrix expressed by Equation (3) is related with the crack modes, the crack location and depth, as well as the rotating speed, and all of these factors might have an influence on the propagation characteristics of the elastic waves. In this section, the crack mode will be analyzed firstly, the most suitable mode will be chosen out, and then, the influence of the location and the depth of the transverse crack as well as the rotating speed to the propagation characteristics is thoroughly studied.

The numerical method is used to obtain the eigenvalues of the transfer matrix, and to make clear the relationship between the crack mode and the crack depth with the changing of the propagation characteristics. An experimental rig is built up and experiments are performed accordingly. The rig is shown in Figure 4.

Preprints (www.preprints.org) | NOT PEER-REVIEWED | Posted: 4 October 2018 doi:10.20944/preprints201810.0068.v1

Peer-reviewed version available at Appl. Sci. 2018, 8, 2105; doi:10.3390/app8112105

Figure 4. The rig built up for the experiments.

As shown in Figure 4, the shaft to be tested is supported by two sliding bearings which are fixed on a steel base, and the shaft is driven by a servo motor (2.5Kw, 3000RPM). The acceleration sensors (PCB LW16 series) are fixed on the bearings and on the steel base. An exciter is used to stimulate the elastic waves in the shaft by acting a pulse force to the shaft. The pulse force is measured by a force sensor too.

Suppose that the elastic waves propagate from location x_0 to x_l, and there is only one transverse crack, located at x_c, as shown in Figure 1(b). The linear variation form of the shaft $S(x)=S(0)(1+x/L)$ is chosen in the paper. As for other variation forms, similar analysis can be performed in the same manner. The radius of the little end ($x_0=0$) of the selected shaft is 15.00mm and the area ratio of the shaft is $S(x_l)/S(x_0)=2/1$. A uniform shaft having the same mass with the non-uniform shaft is also studied for better comparison, the diameter of the uniform shaft is 36.74mm, which can be easily calculated. The material of shaft is 45# steel, the density ρ is $7.8\times10^3\,\mathrm{kg\cdot m^{-3}}$, the elastic modulus E is 2.06×10^{11}Pa, the Poisson's ratio ν is 0.3 and the shear modulus G is 80GPa. The study is divided into 4 parts, as shown in Table 1.

Table 1. The numerical and experiment scheme.

	Location of the crack (x_c)	**Depth of the crack (a)**	**RPM**(Hz)
Part 1	$0.3L$	$0.5R_c$	50
Part 2	$0.3L$	$0.1R_c$, $0.2R_c$, $0.3R_c$, $0.4R_c$, $0.5R_c$	50
Part 3	$0.1L$,$0.2L$,$0.3L$,$0.4L$,$0.5L$, $0.6L$,$0.7L$, $0.8L$,$0.9L$	$0.5R_c$	50
Part 4	$0.3L$	$0.5R_c$	0, 10, 20, 30, 40, 50

Table 1 shows the scheme for the numerical simulation and the experimental analysis. In the table, R_c is the radius of the shaft at location x_c and L is the length of the shaft. Part 1 is for choosing the suitable crack mode, the crack is set to locate at $x_c=0.3L$ with a crack depth $0.5R_c$. Part 2 is to study the relationship between the crack depth and the change of the propagation characteristics, the crack is set to locate at $x_c=0.3L$ with the crack depth $0.1R_c$, $0.2R_c$, $0.3R_c$, $0.4R_c$ and $0.5R_c$. Part 3 is for finding the relationship between the crack location and the change of the propagation characteristics, the crack is set to locate at $x_c=0.1L$, $0.2L$, $0.3L$, $0.4L$, $0.5L$, $0.6L$, $0.7L$, $0.8L$ and $0.9L$ with crack depth $0.5R_c$. In order to avoid possible influence from others, the rotating speeds of the shaft in the first three parts are set to be 3000 rpm (50Hz). Part 4 is for analyzing the relationship between the rotating speed and the change of the propagation characteristics, the crack locates at $0.3L$ with depth $0.5R_c$, and the rotating speeds are set to be 0, 10, 20, 30, 40 and 50Hz.

3.1 Crack Mode

3.1.1 Numerical Analysis

Substituting the properties data as well as other parameters into Equation (3), the transfer matrix can be derived. It can be noticed that the matrix is an exponential one which means the

analytical solution of the eigenvalues can't be obtained. Thus, the MATLAB software is used in this paper to gain the numerical solutions of the eigenvalues. The propagation characteristics of the elastic wave can then be derived from the eigenvalues, and shown in Figure 5.

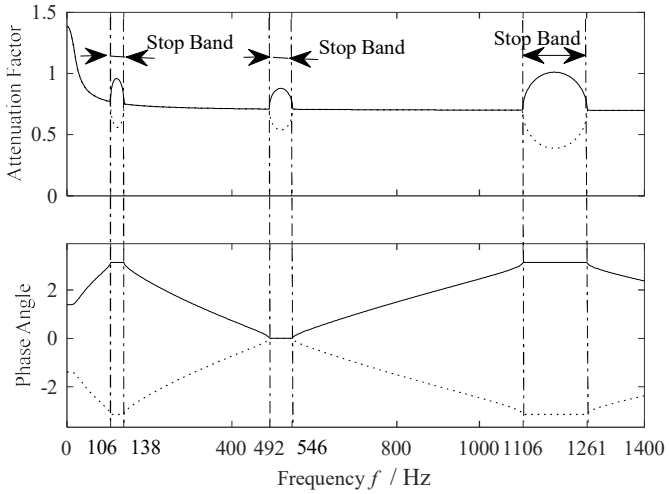

(a)

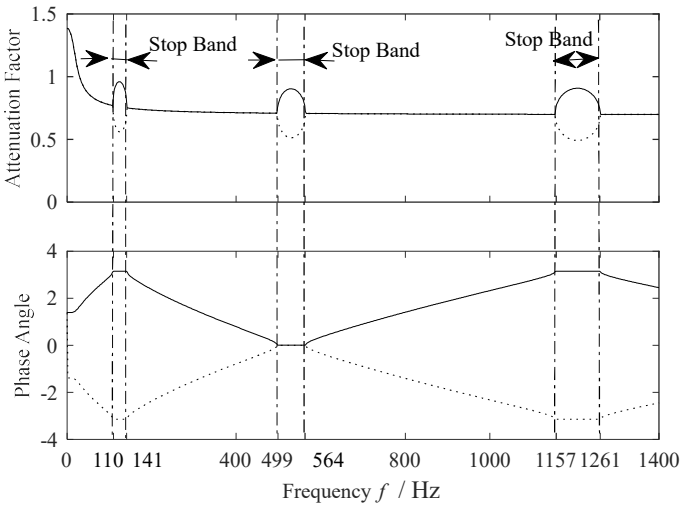

(b)

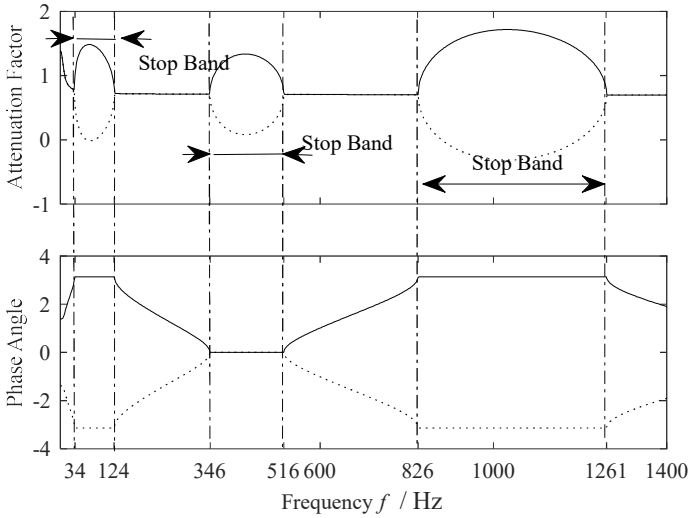

(c)

Figure 5. Numerical propagation constants derived from three different modes, (a) is derived with Mode I, (b) is derived with mode II and (c) is derived with mode III.

Figure 5(a), 5(b) and 5(c) are the numerical propagation constants derived with mode I, II and III, respectively. The upper part of each figure shows the attenuation factor varying as time, and the lower part indicates the phase angle varying as time. The stop bands are identified in the figure, according to the definition that the band with phase angle equals 0 or ±π is a stopband. All the stopbands are listed in Table 2 for easy comparison.

Table 2. Numerical stopbands derived from different crack modes.

Crack mode	Stopbands (Hz)
Mode I	[106, 138], [492, 546], [1100, 1261]
Mode II	[110, 141], [499, 564], [1157, 1261]
Mode III	[34, 124], [346, 516], [826, 1261]

It can be known from the above table that different modes will result in different stopbands. The results for Mode I and Mode II are similar, but they are obviously different with the results for Mode III. It's of great necessary to choose the most suitable mode.

3.1.2 Experimental Analysis

Experiments are performed in the rig according to the conditions listed in Table 2. The shaft is driven by a servo motor and rotate at 3000 rpm. The stimulator gives the shaft an instant force to stimulate the elastic waves, and then the wave begins to propagate from the end to the other. Acceleration sensors are set on both ends of the shaft, which can capture the waves. As mentioned before, the uniform shaft having the same mass with the non-uniform shaft is also studied here for deducing the propagation constants by comparison. The propagation characteristics of the elastic waves in the real shaft can be deduced by comparing the spectrum of the signals. The result is shown in Figure 6.

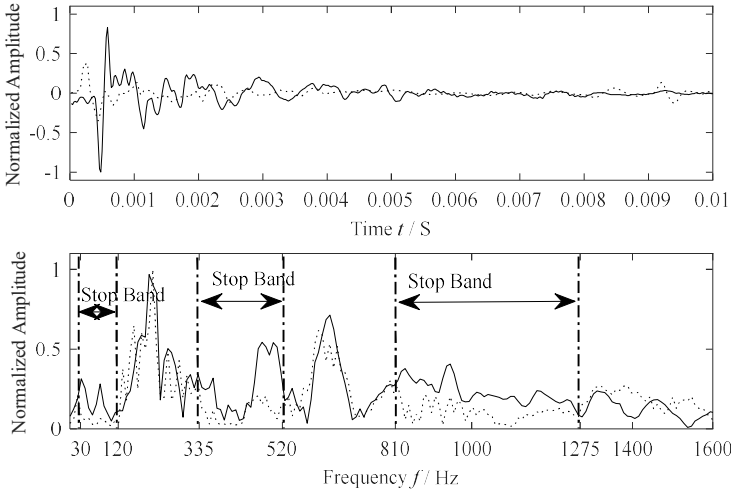

Figure 6. Experimental Stop Bands derived by spectrum comparison.

As shown in the upper of Figure 6, the time history of the acceleration signals at location x_l shown in Figure 1 is truncated to 0.01s for analysis, and these signals are captured after propagating through the shaft. The lower part is the spectrum of the time history, and the spectrum are derived by FFT (Fast Fourier Transform). The real lines stand for the uniform shaft while the dotted ones stand for the non-uniform shaft. In the spectrum curve, if the full line is higher than the dotted line, which means the energy distributed in the range is much higher, then, the corresponding range can

Preprints (www.preprints.org) | NOT PEER-REVIEWED | Posted: 4 October 2018 doi:10.20944/preprints201810.0068.v1

Peer-reviewed version available at Appl. Sci. 2018, 8, 2105; doi:10.3390/app8112105

be treated as a stopband. In the above figure, three stopbands can be found, and they are [30, 120], [335, 520] and [810, 1275] separately. Compared with the numerical results listed in Table 2, it can be found that the experimental result matches well with the result deduced with crack mode III, though there are errors between the two. Thus, it can be determined that mode III is the most suitable for the shaft in the experiments.

3.2 Crack Location

3.2.1 Numerical Analysis

In this subsection, the influence of the location of the transverse crack to the propagation characteristics of the elastic waves is studied. Crack mode III is chosen for the aforementioned reason. The non-uniform shaft is still the same one but with different crack locations as listed in Table 1. Similarly, substituting all the parameters into Equation (3), the transfer matrix can then be derived. The propagation characteristics of the elastic waves are obtained in a numerical manner, and the results are shown in Figure 7.

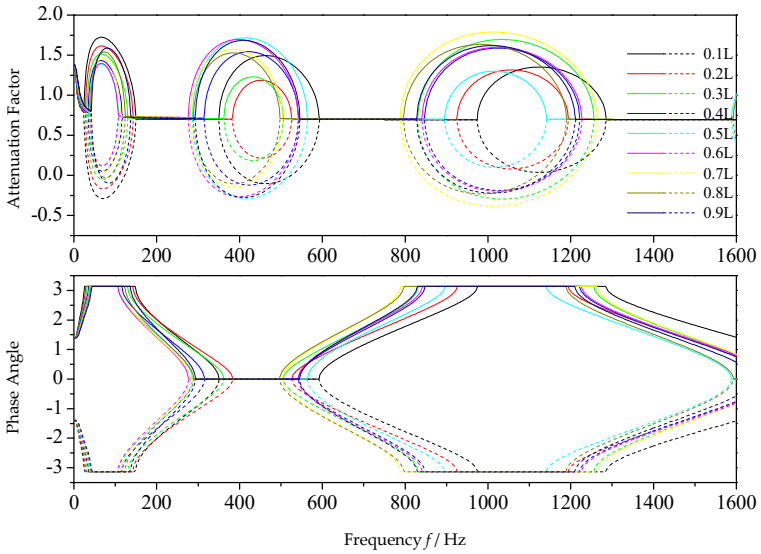

Figure 7. Numerical propagation constants derived from different crack locations.

As can be seen in the figure, the results for different locations are indicated by different colors, and the real line and the dotted line of the same color are a pair of conjunct propagation constant. Obviously, the propagation characteristics are affected by the locations. The stopbands are not signed out in the figure for clearance, instead, all of which are listed in Table 3.

Table 3. Numerical stopbands derived at different crack locations.

Locations	Stopbands (Hz)
0.1*L*	[26, 148], [352, 592], [976, 1284]
0.2*L*	[30, 142], [384, 526], [926, 1194]
0.3*L*	[34, 124], [346, 516], [826, 1261]
0.4*L*	[36, 116], [316, 542], [848, 1220]
0.5*L*	[38, 106], [288, 562], [896, 1140]
0.6*L*	[40, 106], [278, 540], [842, 1226]
0.7*L*	[40, 112], [282, 502], [790, 1262]
0.8*L*	[42, 122], [290, 496], [798, 1188]
0.9*L*	[44, 136], [294, 544], [830, 1210]

It can be seen from Table 3 that there are three stopbands for each location. The widths of the stopbands fluctuate as the location. For locations from 0.1*L* to 0.9*L*, the bandwidth of the first

stopband becomes narrow firstly, it will reach a minimum at the middle of the shaft, and then it will become wider. For the bandwidth of the second stopband, it will be the widest when the crack locates at 0.5*L*. And, the bandwidth of the third stopbands will the largest for locations 0.3*L* and 0.7*L*. The second and the third stopbands vary as the locations more obviously than the first one.

3.3.2 Experimental Analysis

Experiments are performed in the rig according to the conditions listed in Table 1. As mentioned before, the uniform shaft having the same mass with the non-uniform shaft is also studied here for deducing the propagation characteristics by comparison. The results of the experiments are shown in Figure 8.

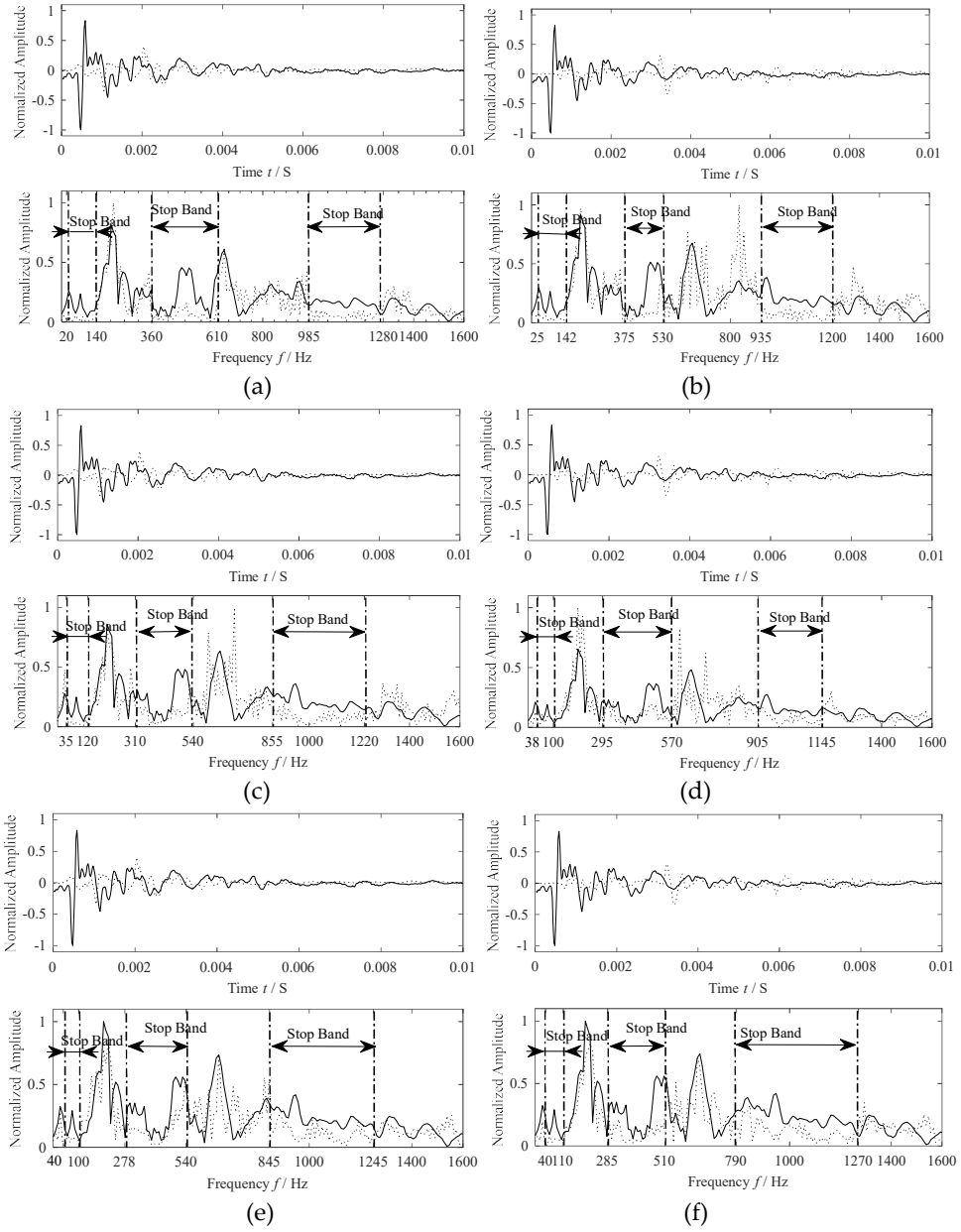

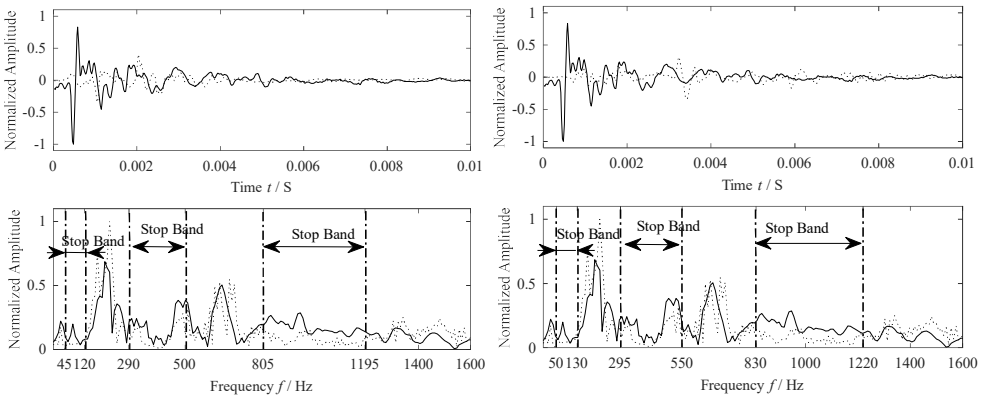

Figure 8. Experimental Stop Bands derived at different crack locations, where (a) is for location 0.1*L*, (b) is for location 0.2*L*, (c) is for location 0.4*L*, (d) is for location 0.5*L*, (e) is for location 0.6*L*, (f) is location 0.7*L*, (g) is for location 0.8*L* and (h) is for location 0.9*L*.

The time history of the acceleration signals is truncated to 0.01s for all cases. and these signals are captured after propagating through the shaft. The real lines stand for the uniform shaft while the dotted ones stand for the non-uniform shaft. All the stopbands shown in Figure 8 are listed in Table 4 for comparison. The case of location 0.3*L* has already been studied in Subsection 3.1 and the result of which is listed in the table too.

Table 4. Experimental stopbands derived from different crack locations.

Locations	Stopbands (Hz)
0.1*L*	[20, 140], [360, 610], [985, 1280]
0.2*L*	[25, 142], [375, 530], [935, 1200]
0.3*L*	[30, 120], [335, 520], [810, 1275]
0.4*L*	[35, 120], [310, 540], [855, 1220]
0.5*L*	[38, 100], [295, 570], [905, 1145]
0.6*L*	[40, 100], [278, 540], [845, 1245]
0.7*L*	[40, 110], [285, 510], [790, 1270]
0.8*L*	[45, 120], [290, 500], [805, 1195]
0.9*L*	[50, 130], [295, 550], [830, 1220]

From Table 4, it can be found that the experimental results match well with the numerical ones. The bandwidth of the first stopbands varies slightly, while the bandwidths of the second and third stopband fluctuate as the location. For the second stopband, the bandwidth of which will reach a peak when the crack locates at 0.5*L*, while, the bandwidth of the third stopbands will reach a peak at locations 0.3*L* and 0.7*L*. If the shaft is long enough, more accurate relationship can be found out. The bandwidth of the stopband can reflect the location changing of the crack, which may be helpful to locate a crack.

3.3 Crack Depth

3.3.1 Numerical Analysis

It is researched in this subsection that how the depth of transverse crack affects the propagation characteristics of the elastic waves. Crack mode III is adopted here for the conclusion of Subsection 3.1. The non-uniform shaft is still the same one but with different crack depths as listed in Table 1. Similarly, substituting all the parameters into Equation (3), the transfer matrix is then derived. And the numerical method is adopted to obtain the numerical results of the propagation characteristics of the elastic waves, the numerical results are shown in Figure 9.

Preprints (www.preprints.org) | NOT PEER-REVIEWED | Posted: 4 October 2018 doi:10.20944/preprints201810.0068.v1

Peer-reviewed version available at Appl. Sci. 2018, 8, 2105; doi:10.3390/app8112105

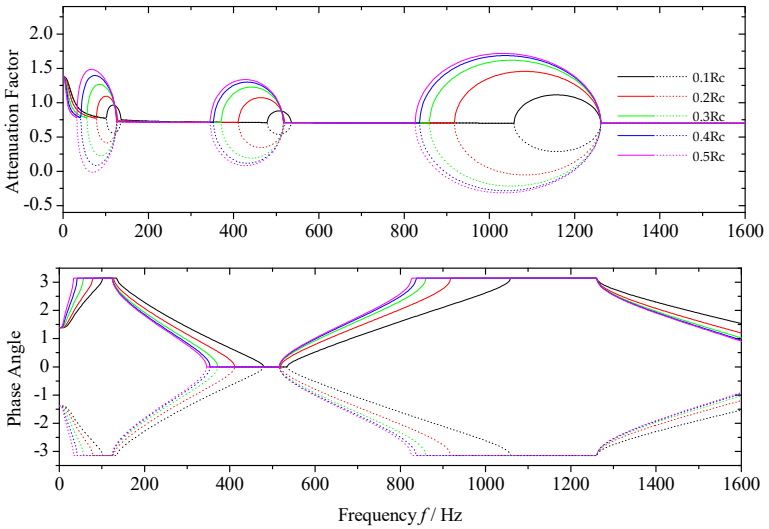

Figure 9. Numerical propagation constants derived from different crack depths.

As can be seen in Figure 9, the numerical results derived at different depth are signed by different symbols and colors, while the real line and the dotted line of the same color are a pair of conjunct propagation constants. The stopbands are not directly identified in the figure for clarity, instead, they are listed in Table 5.

Table 5. Numerical Stopbands derived at different crack depths.

Depth (a/R_c)	Stopbands (Hz)
0.1	[102, 134], [480, 534], [1060, 1261]
0.2	[80, 126], [412, 518], [918, 1261]
0.3	[58, 124], [372, 516], [860, 1261]
0.4	[42, 124], [354, 516], [838, 1261]
0.5	[34, 124], [346, 516], [828, 1261]

It can be deferred that the three stopbands vary as the depth: the bandwidth of the three stopbands become wider as the increase of the depth of the transverse crack, while the central frequency of the stopbands become lower as the increase of the depth of the crack.

3.3.2 Experimental Analysis

Experiments are performed in the rig according to the conditions listed in Table 2. The propagation characteristics of the elastic waves in the real shaft can be deduced by comparing the spectrum of the signals. The results are shown in Figure 10.

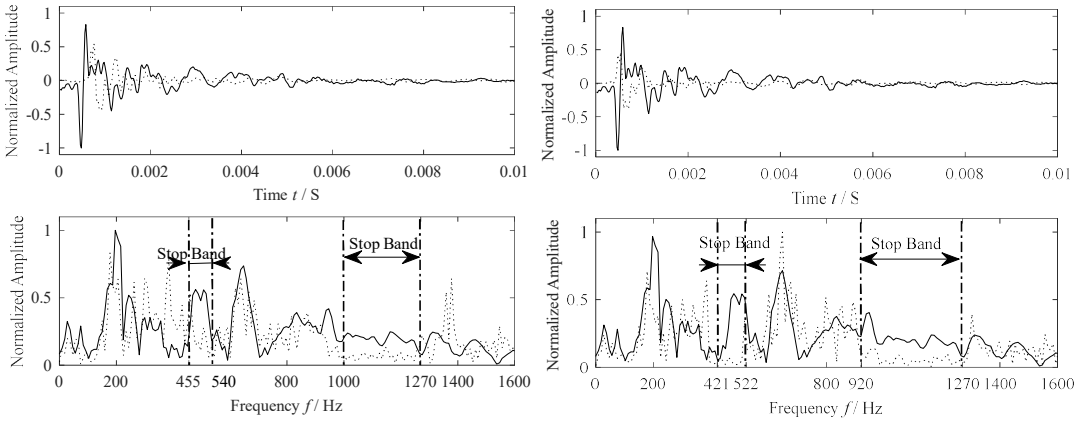

Preprints (www.preprints.org) | NOT PEER-REVIEWED | Posted: 4 October 2018 doi:10.20944/preprints201810.0068.v1

Peer-reviewed version available at Appl. Sci. 2018, 8, 2105; doi:10.3390/app8112105

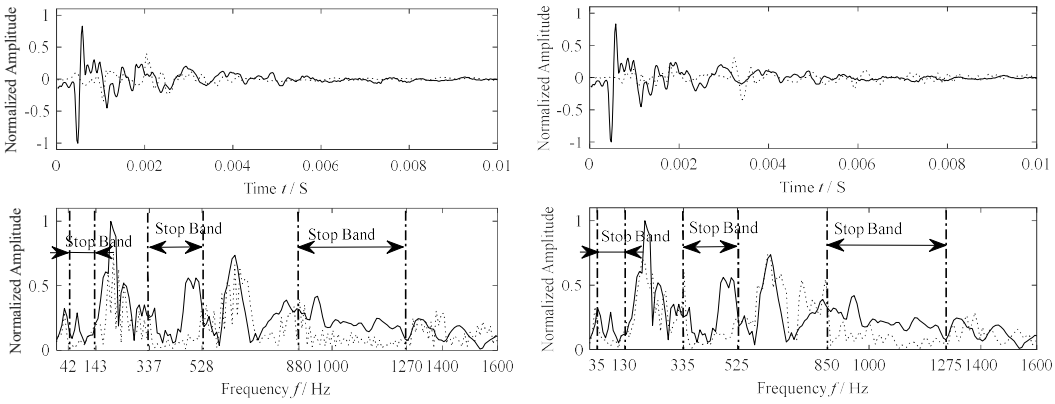

(c) (d)

Figure 10. Experimental stopbands derived from different crack depth, where (a) is for the case a/R_c=0.1, (b) is for the case a/R_c=0.2, (c) is for the case a/R_c=0.3 and (d) is for the case a/R_c=0.4.

Figure 10 shows the experimental stop bands derived at different crack depth (a/R_c=0.1, 0.2, 0.3, 0.4). As mentioned before, the uniform shaft having the same mass with the non-uniform shaft is also studied here for deducing the propagation characteristics by comparison. Similarly, the time history of the acceleration signals is truncated to 0.01s. The real lines stand for the uniform shaft while the dotted ones stand for the non-uniform shaft. As for the crack depth a/R_c=0.5, the experimental results have been shown in Figure 6. All the experimental results are listed in Table 6.

Table 6. Experimental stopbands derived at different crack depths.

Depth (a/R_c)	Stopbands (Hz)
0.1	[455, 540], [1000, 1270]
0.2	[421, 522], [920, 1270]
0.3	[42, 143], [337, 528], [880, 1270]
0.4	[35, 130], [335, 525], [850, 1275]
0.5	[30, 120], [335, 520], [810, 1275]

As can be seen in Table 6, there are two stopbands for the cases 0.1 and 0.2, but the number becomes three for the cases 0.3, 0.4 and 0.5. All the stopbands become wider as the increase of the depth, and the central frequency will be lower. The results of the experiments match well with the numerical ones. For the case 0.1 and 0.2, the lower stopbands are missing, the main reason is due to the constriction of experimental conditions. Thus, it can be verified that the bandwidth of the three stopbands become wider as the increase of the depth of the transverse crack, while the central frequency of the stopbands become lower and lower at same time. The bandwidth and the central frequency can be used to indicate the depth of a crack.

3.4 Rotating Speed

3.4.1 Numerical Analysis

It is researched in this subsection that how the depth of transverse crack affects the propagation characteristics of the elastic waves. Crack mode III is adopted here too. The non-uniform shaft is still the same one but with different rotating speeds as listed in Table 1. Similarly, substituting all the parameters into Equation (3), the transfer matrix is then be derived. And, numerical method is adopted to obtain the numerical results of the propagation constants of the elastic waves, the numerical results are shown in Figure 11.

Preprints (www.preprints.org) | NOT PEER-REVIEWED | Posted: 4 October 2018 doi:10.20944/preprints201810.0068.v1

Peer-reviewed version available at Appl. Sci. 2018, 8, 2105; doi:10.3390/app8112105

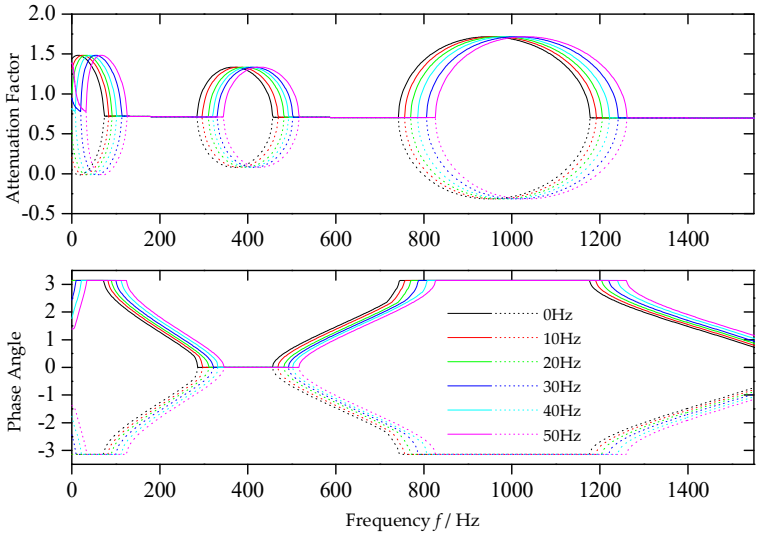

Figure 11. Numerical propagation constants derived from different rotating speeds.

As can be seen in the figure, the stopbands are affected by the rotating speeds. Different colors indicate different rotating speeds, while the real line and the dotted line of the same color are a pair of conjunct propagation constants. All the bands are listed in Table 7 for better comparison.

Table 7. Numerical stopbands derived from different rotating speeds.

RPM	Stopbands (Hz)
0Hz	[0, 71], [285, 455], [743, 1181]
10Hz	[0, 82], [297, 467], [758, 1196]
20Hz	[0, 91], [309, 479], [772, 1210]
30Hz	[8, 100], [322, 492], [787, 1225]
40Hz	[23, 113], [332, 502], [808, 1243]
50Hz	[33, 124], [346, 516], [826, 1261]

It can be found in Table 7 that there are three stopbands for each case. The central frequencies of the second and the third stopbands will be higher and higher as the increase of the rotating speed, while the bandwidth of which remain the same, and they are 170Hz, 435Hz, separately. For the first stopband, it starts with 0Hz when the rotating speed is lower than 30, while the bandwidth will be the same for the cases 30Hz, 40Hz and 50Hz. It can be thought that the central frequency and bandwidth of the first stopband vary the same manner as the other two. The rotating speed will shift up the stopbands as the increase of the rotating speed, while, without changing the bandwidth.

3.4.2 Experimental Analysis

Experiments are performed in the rig according to the conditions listed in Table 2. The uniform shaft having the same mass with the non-uniform shaft is also studied. The shafts will rotate at different speeds. The propagation characteristics will be obtained by comparing the spectrum of the signals. The results of the experiments are shown in Figure 12.

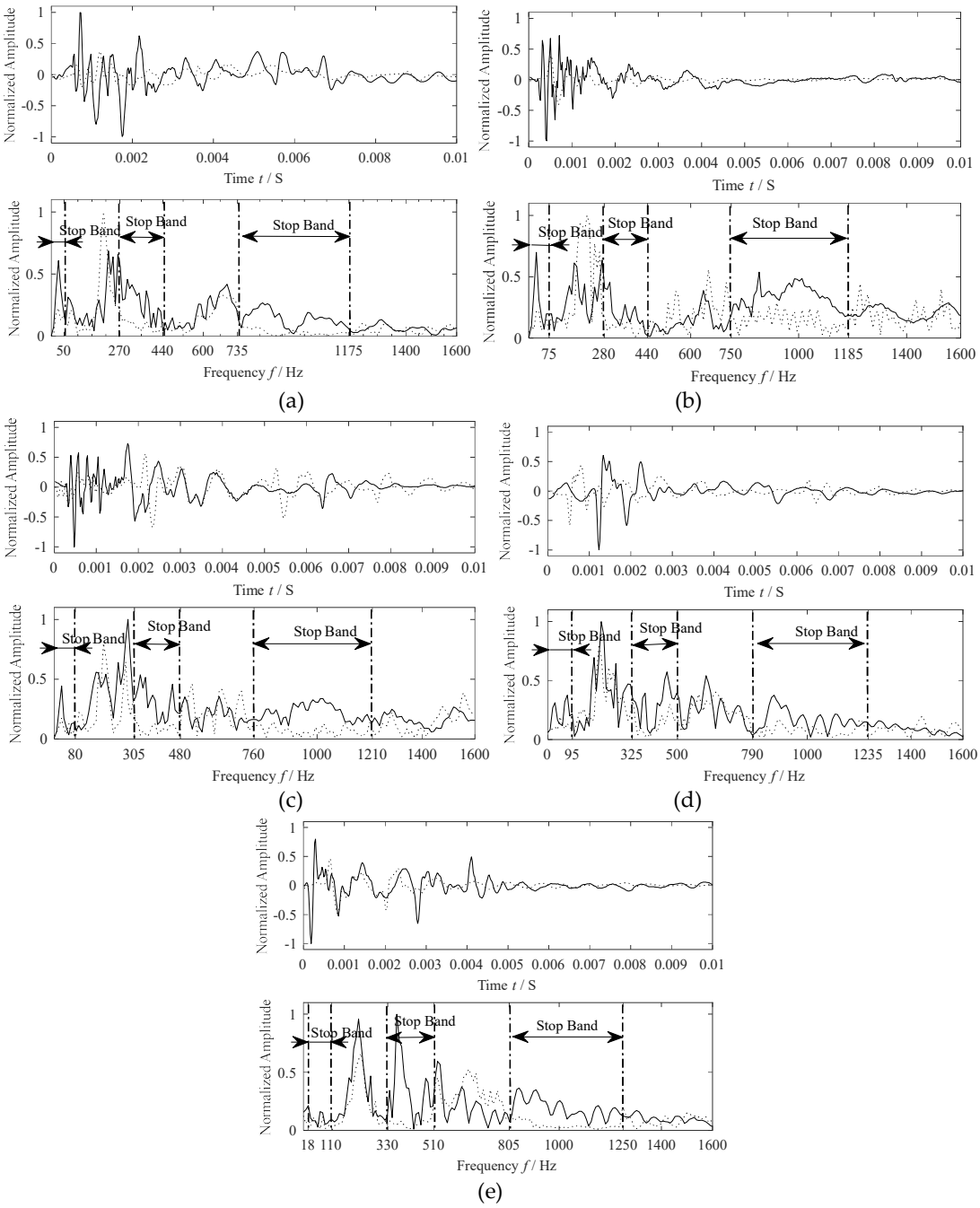

Figure 12. Experimental propagation characteristics derived from different rotating speeds, where (a) is for 0Hz, (b) is for 10Hz, (c) is for 20 Hz, (d) is for 30 Hz and (e) is for 40Hz.

Figure 12 shows the experimental stop bands derived at different rotating speeds. Similarly, the time history of the acceleration signals from both the uniform and non-uniform shafts is truncated to 0.01s. The real lines and the dotted lines stand for the uniform shaft and the non-uniform shaft, separately. As for the rotating speed 50Hz, the experimental results have been shown in Figure 6. All the experimental results are listed in Table 8.

Table 8. Experimental stopbands derived from different rotating speeds.

RPM	Stopbands (Hz)
0Hz	[0, 50], [270, 440], [735, 1175]

10Hz	[0, 75], [280, 450], [750, 1185]
20Hz	[0, 80], [305, 480], [760, 1210]
30Hz	[0, 95], [325, 500], [790, 1235]
40Hz	[18, 110], [330, 510], [805, 1250]
50Hz	[30, 120], [335, 520], [810, 1275]

From Table 8, it can be found that the experimental results match well with the numerical ones. The central frequencies of the three stopbands will be higher and higher as the increase of the rotating speed, while the bandwidth of which remain the same. The shift up of the stopband can be treated as the increase of the rotating speed, which can help to distinguish the changing in crack depth.

4.Conlusion

The propagation characteristics of the elastic waves propagating in a non-uniform shaft with a transverse crack is studied with considering three individual crack modes in this paper. The influence of crack mode, crack location, crack depth and the rotating speed to propagation characteristics is thoroughly studied. It's found that:

(1) Different crack mode will lead to different propagation characteristics. For a shaft or shaft-like component, crack mode selection according to the external loadings is necessary and mode III is the most suitable crack mode in this paper.

(2) The location of the crack will make the stopbands fluctuating. The bandwidth of second stopband will reach a peak when the crack locates at the middle location 0.5*L*, while, the bandwidth of the third stopband will reach a peak at locations 0.3*L* and 0.7*L*. The bandwidth can be helpful to locate the transverse crack.

(3) The bandwidth of the stopbands become wider as the increase of the depth of the transverse crack while the central frequency of the stopbands become lower as the increase of the depth of the crack. The central frequency and the bandwidth can be used for transverse crack detection.

(4) The increase of rotating speed will shift up the three stopbands, while the bandwidth of them remain the same.

Only one single mode is considered when studying the propagation characteristics of the elastic waves in this paper. The cracks may have combined modes in real applications. The combination of the three basic modes as well as the multi-cracks case need to be studied further.

Author Contributions: Y.W developed the original concept and wrote the paper. X.S performed the experiments. Q.L & X.S conducted experimental data analysis. W.C. verified the results.

Acknowledgements: This research was supported by National Natural Science Foundation of China with grant No. 51505430, Public Project of Zhejiang Province with grant No. LGG18E050021, NSFC-Zhejiang Joint Fund for the Integration of Industrialization and Informatization with grand No. U1709210, International S&T Cooperation Program of China with grant No. 2015DFA71400.

Conflicts of Interest: The authors declare no conflict of interest.

References

1. Gómez, M.J.; Castejón, C.; García-Prada, J.C. Crack detection in rotating shafts based on 3× energy: Analytical and experimental analyses. *Mechanism and Machine Theory* **2016**, *96*, 94-106, doi:10.1016/j.mechmachtheory.2015.09.009.
2. Neves, A.C.; Simões, F.M.F.; Pinto da Costa, A. Vibrations of cracked beams: Discrete mass and stiffness models. *Computers & Structures* **2016**, *168*, 68-77, doi:10.1016/j.compstruc.2016.02.007.
3. Oswald-Tranta, B. Induction Thermography for Surface Crack Detection and Depth Determination. *Applied Sciences* **2018**, *8*, 257, doi:10.3390/app8020257.
4. Bovsunovsky, A.P. Efficiency analysis of vibration based crack diagnostics in rotating shafts. *Engineering Fracture Mechanics* **2017**, *173*, 118-129, doi:10.1016/j.engfracmech.2017.01.014.

5. Lee, J.W.; Lee, J.Y. A transfer matrix method capable of determining the exact solutions of a twisted Bernoulli–Euler beam with multiple edge cracks. *Applied Mathematical Modelling* **2017**, *41*, 474-493, doi:http://dx.doi.org/10.1016/j.apm.2016.09.013.
6. Stawiarski, A.; Barski, M.; Pająk, P. Fatigue crack detection and identification by the elastic wave propagation method. *Mechanical Systems and Signal Processing* **2016**, *89*, 119-130, doi:10.1016/j.ymssp.2016.08.023.
7. Vishwakarma, M.; Purohit, R.; Harshlata, V.; Rajput, P. Vibration Analysis & Condition Monitoring for Rotating Machines: A Review. *Materials Today: Proceedings* **2017**, *4*, 2659-2664, doi:http://dx.doi.org/10.1016/j.matpr.2017.02.140.
8. Silani, M.; Ziaei-Rad, S.; Talebi, H. Vibration analysis of rotating systems with open and breathing cracks. *Applied Mathematical Modelling* **2013**, *37*, 9907-9921, doi:10.1016/j.apm.2013.05.040.
9. Chen, H.; Chen, P.; Chen, W.; Wu, C.; Li, J.; Wu, J. Wind Turbine Gearbox Fault Diagnosis Based on Improved EEMD and Hilbert Square Demodulation. *Applied Sciences* **2017**, *7*, 128, doi:10.3390/app7020128.
10. Barad, K.H.; Sharma, D.S.; Vyas, V. Crack Detection in Cantilever Beam by Frequency based Method. *Procedia Engineering* **2013**, *51*, 770-775, doi:10.1016/j.proeng.2013.01.110.
11. Bahrami, A.; Teimourian, A. Free vibration analysis of composite, circular annular membranes using wave propagation approach. *Applied Mathematical Modelling* **2015**, *39*, 4781-4796, doi:10.1016/j.apm.2015.03.057.
12. Jingpin, J.; Xiangji, M.; Cunfu, H.; Bin, W. Nonlinear Lamb wave-mixing technique for micro-crack detection in plates. *NDT & E International* **2017**, *85*, 63-71, doi:http://dx.doi.org/10.1016/j.ndteint.2016.10.006.
13. Nobrega, E.D.; Gautier, F.; Pelat, A.; Dos Santos, J.M.C. Vibration band gaps for elastic metamaterial rods using wave finite element method. *Mechanical Systems and Signal Processing* **2016**, *79*, 192-202, doi:10.1016/j.ymssp.2016.02.059.
14. Qu, L.; Ding, X.; Zheng, C.; Liu, H. An analytical solution for wave propagation in a square pile due to transient point load. *Computers and Geotechnics* **2017**, *83*, 77-82, doi:10.1016/j.compgeo.2016.11.002.
15. Tavasoli, O.; Ghazavi, M. Wave propagation and ground vibrations due to non-uniform cross-sections piles driving. *Computers and Geotechnics* **2018**, *104*, 13-21, doi:10.1016/j.compgeo.2018.08.010.
16. Joglekar, D.M.; Mitra, M. Analysis of flexural wave propagation through beams with a breathing crack using wavelet spectral finite element method. *Mechanical Systems and Signal Processing* **2016**, *76-77*, 576-591, doi:10.1016/j.ymssp.2016.02.010.
17. Joglekar, D.M.; Mitra, M. Nonlinear analysis of flexural wave propagation through 1D waveguides with a breathing crack. *Journal of Sound and Vibration* **2015**, *344*, 242-257, doi:10.1016/j.jsv.2015.01.038.
18. Nandakumar, P.; Shankar, K. Structural crack damage detection using transfer matrix and state vector. *Measurement* **2015**, *68*, 310-327, doi:10.1016/j.measurement.2015.03.010.
19. Behzad, M.; Ghadami, A.; Maghsoodi, A.; Michael Hale, J. Vibration based algorithm for crack detection in cantilever beam containing two different types of cracks. *Journal of Sound and Vibration* **2013**, *332*, 6312-6320, doi:10.1016/j.jsv.2013.07.003.
20. Liu, J.; Zhu, W.D.; Charalambides, P.G.; Shao, Y.M.; Xu, Y.F.; Fang, X.M. A dynamic model of a cantilever beam with a closed, embedded horizontal crack including local flexibilities at crack tips. *Journal of Sound and Vibration* **2016**, *382*, 274-290, doi:10.1016/j.jsv.2016.04.036.

21. Broda, D.; Pieczonka, L.; Hiwarkar, V.; Staszewski, W.J.; Silberschmidt, V.V. Generation of higher harmonics in longitudinal vibration of beams with breathing cracks. *Journal of Sound and Vibration* **2016**, *381*, 206-219, doi:10.1016/j.jsv.2016.06.025.
22. Giannopoulos, G.I.; Georgantzinos, S.K.; Anifantis, N.K. Coupled vibration response of a shaft with a breathing crack. *Journal of Sound and Vibration* **2015**, *336*, 191-206, doi:10.1016/j.jsv.2014.09.037.
23. Tada, H.; Paris, P.C.; Irwin, G.R. *The Stress Analysis of Cracks Handbook*; Del Research Corporation, 2000.
24. Saboori, B.; Ayatollahi, M.R.; Torabi, A.R.; Berto, F. Mixed mode I/III brittle fracture in round-tip V-notches. *Theoretical and Applied Fracture Mechanics* **2016**, *83*, 135-151, doi:10.1016/j.tafmec.2015.12.002.
25. Isidoro, J.; Martins, R.F. Calculation of Stress Intensity Factors K I , K II and K III of Cracked Components Submitted to Flexural and Torsional Loads. *Procedia Engineering* **2016**, *160*, 131-136, doi:10.1016/j.proeng.2016.08.872.
26. Predan, J.; Močilnik, V.; Gubeljak, N. Stress intensity factors for circumferential semi-elliptical surface cracks in a hollow cylinder subjected to pure torsion. *Engineering Fracture Mechanics* **2013**, *105*, 152-168, doi:10.1016/j.engfracmech.2013.03.033.
27. Gan, C.; Wei, Y.; Yang, S. Longitudinal wave propagation in a rod with variable cross-section. *Journal of Sound and Vibration* **2014**, *333*, 434-445, doi:http://dx.doi.org/10.1016/j.jsv.2013.09.010.
28. Wei, Y. Equations of motion and propagation characteristics of elastic waves propagating in rods and rotating shafts with variable cross-section. PhD, Hangzhou: Zhejiang University, 2014.
29. Toso, M. Wave propagation in rods, shells, and rotating shafts with non-uniform geometry. PhD, University of Maryland, Maryland, 2004.
30. Gayen, D.; Chakraborty, D. Variation of Local Flexibility Coefficients of Functionally Graded Cracked Shaft. *Procedia Engineering* **2016**, *144*, 1443-1450, doi:10.1016/j.proeng.2016.05.176.
31. Tsai, T.C.; Wang, Y.Z. Vibration analysis and diagnosis of a cracked shaft. *Journal of Sound and Vibration* **1996**, *192*, 607-620, doi:https://doi.org/10.1006/jsvi.1996.0209.